



Internal erosion of a gap-graded soil and influences on the critical state

Shijin Li^{1,4} · Adrian R. Russell² · David Muir Wood³

Received: 16 July 2023 / Accepted: 11 January 2024
© The Author(s) 2024

Abstract

Water retaining structures are critical elements of civil infrastructure. Internal erosion of soils forming the containment structures may occur progressively and lead to expensive maintenance costs or failures. The strength, stress–strain behavior and critical state of soils which have eroded, as well as the characteristics of the erosion, may be affected by hydraulic gradient, confining stress and relative density of the soil at the start of the erosion. Here, erosion and triaxial tests have been conducted on gap-graded soil samples. The tests and results are novel as the samples were prepared to be homogenous post-erosion and prior to triaxial testing by adopting a new sample formation procedure. The post-erosion homogeneity was evaluated in terms of particle size distribution and void ratio along a sample's length. The erosion-induced mechanical property changes can then be linked to a measure of initial state, more reliably than when erosion causes samples to be heterogeneous. The results show that erosion causes the critical state line in the compression plane to move upwards. The movement is lesser than the increase in void ratio caused by erosion. The state parameter is therefore reduced, consistent with the soil's reduced peak strength and its less dilative response. Regarding the erosion characteristics, the flow rate decreases with the increase in initial relative density or effective stress, but increases with the increase in the hydraulic gradient being applied. The cumulative eroded soil mass increases with the increase in hydraulic gradient and decreases with the increase in initial density and effective confining stress.

Keywords Critical state · Gap-graded soil · Internal erosion · Triaxial test

1 Introduction

Water retaining structures made from soil embankments are expected to perform safely for many decades. However, internal erosion of the soils forming the embankments may occur and lead to expensive maintenance costs or, in extreme cases, collapse. More than 35% of embankment dam failures and dysfunctions are caused by internal erosion [19, 66].

Researchers have studied the erosion characteristics, and the mechanical consequences of erosion, by conducting triaxial tests on samples having different initial particle size distributions (PSDs) attained through varying amounts of erosion [7, 12, 26, 27, 43, 49, 55, 65, 71]. They found internal erosion not only caused a change to the PSD, but also an increase in void ratio (e) and permeability (k) and, importantly, alterations to mechanical properties including strengths and stress–strain behaviors.

✉ Adrian R. Russell
a.russell@unsw.edu.au

Shijin Li
Shijin_li@outlook.com

David Muir Wood
d.muirwood@dundee.ac.uk

¹ School of Civil Engineering, Tianjin University, Tianjin, China

² Centre for Infrastructure Engineering and Safety, School of Civil and Environmental Engineering, The University of New South Wales, Sydney, NSW 2052, Australia

³ School of Science and Engineering, University of Dundee, Dundee, UK

⁴ Institute of Mechanics, Materials and Civil Engineering, Université Catholique de Louvain, Louvain-la-Neuve, Belgium

These triaxial tests have a common limitation. The erosion of samples inside the apparatus, prior to triaxial testing, caused heterogeneous PSDs to form [12, 27, 28]. This makes it difficult to relate the test results to a measure of the eroded soil sample's state, as key properties like the PSD and e are different along a sample's length. Li et al. [37] attempted to overcome this problem and presented a novel soil sample formation procedure, which results in homogeneous PSDs and e along a sample's length. They observed samples with homogeneous post-erosion PSDs and e exhibited slightly higher strengths than those which were heterogeneous.

The main objective of this paper is to better understand the mechanical consequences of different amounts of erosion in a gap-graded soil, especially related to the soil's stress-strain behavior and critical state. Triaxial tests on eroded samples with homogeneous PSDs are used. The erosion characteristics under different initial conditions are also observed. Different amounts of internal erosion are realized by controlling either the hydraulic gradient or duration of seepage.

A feature that makes these results of greater interest to others in the literature is that prior to triaxial shearing, the soil samples which experienced internal erosion had homogeneous PSDs and e along their lengths. This means the results can be more reliably linked to measures of state, including e , state parameter and a grading state index [47]. The grading state index is defined as the ratio of areas under the current and a limiting particle size distribution curve. It has a value in the range 0 to 1.

The results may be used to inform discrete element studies and validate their numerical outputs [14, 20, 21, 48, 56, 70, 74]. The results also provide information that may assist dam owners, and their professional advisors, when understanding the mechanical consequences of internal erosion.

2 Apparatus, test soil and sample formation

Triaxial erosion tests may be conducted to study the initiation, rate of progression and characteristics (effluent turbidity, cumulative eroded mass loss) of internal erosion, as well as sample volume change, the post-erosion PSD and the mechanical consequences [12, 13, 26, 27, 37, 43, 49, 55, 65, 71].

The triaxial erosion testing procedure used in this study is broadly similar that that used by others, with the exception of the sample formation method. It contained four steps: (a) saturation and isotropic consolidation of a sample inside the apparatus; (b) internal erosion of the sample (the erosion test); (c) the triaxial test and (d) PSD determination.

The equipment configuration (detailed in [37]) is also broadly similar to others [12, 13, 26, 43, 49, 54, 71] and included a constant head water tank that was able to drive seepage through soil samples while inside the triaxial apparatus (Fig. 1). Water was able to seep through the samples in either upward or downward directions, and a bucket collected the seepage water (i.e., the water containing the eroded particles) once it exited the sample. The samples were cylindrical, 200 mm in diameter and 400 mm in height, i.e., with a height-to-diameter ratio of 2. The ratio is commonly used by others [26, 28, 45, 65]. The sample's base pedestal and top cap contained funnel-shaped depressions to enable the seepage water to exit a sample through its ends and pass into the bucket. Perforated stainless steel disks (base mesh and top mesh as shown in Fig. 1) covered each funnel-shaped depression and acted as rigid base and top sample boundaries. The perforations were circular, 2 mm in diameter, and made a grid pattern with a center-to-center spacing of 3 mm. The 2 mm perforation size was sufficiently large to prevent clogging by fine particles. All flow channels and fittings had an internal diameter of 7.5 mm.

A combination of upward and downward seepage stages enabled a more homogeneous sample to be achieved prior to triaxial testing than was found to be possible by unidirectional seepage [7, 12, 27]. Also, introducing seepage in both directions partly compensated for the vertical effective stress variations which accompanying unidirectional seepage [45].

The axial displacement of the sample during shearing was measured using a linear variable differential transformer (LVDT) with a precision of 0.0001 mm. Axial displacement of a sample during erosion, if it occurred, was also measured. The volume change during erosion (if there was any) and shearing were determined by reading the cell and pore volume burettes at regular time intervals. More details are contained in [37].

The soil was formed by mixing three base materials, referred to as 10 mm basalt, 5 mm basalt and silica 60G. The PSDs are shown in Fig. 2. The mass proportions of silt, sand and gravel-sized particles are 26%, 10% and 64%. The wide and gap-graded size range in the mixture is typical of some erodible soils in dam structures and closely resembles some of the internally unstable soil samples investigated by Wan and Fell [64]. The soil, with a fines content (particles smaller than 0.075 mm) of 25%-30%, sits within the transitional range between underfilled and overfilled [58]. The maximum and minimum e values (e_{\max} and e_{\min}) are 0.53 and 0.10, and the specific gravity of the solid particles is $G_s = 2.73$. The values of e_{\max} and e_{\min} were determined according to the procedures specified by ASTM D4254 [4] and ASTM4253 [3], respectively. The small e_{\min} can be attributed to the fines filling the spaces

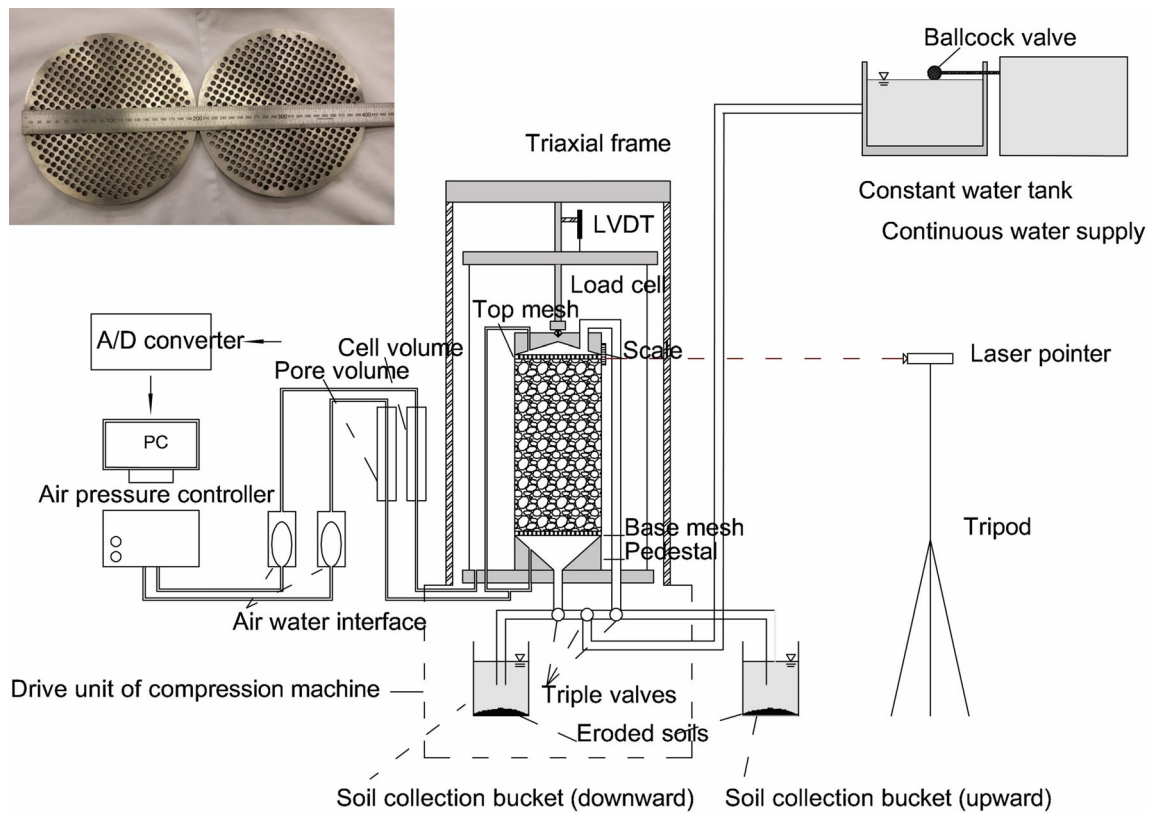


Fig. 1 Schematic diagram of the suffusion triaxial testing system. *A/D*, analog-to-digital

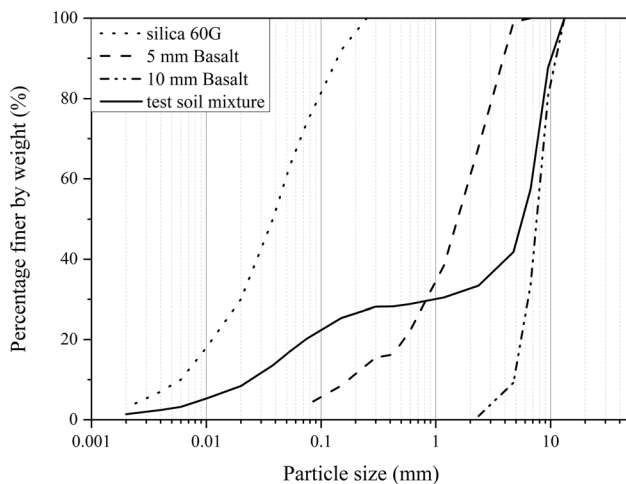


Fig. 2 Particle size distributions of the test soil and its constituents

around the coarse particles efficiently. A similarly small e_{\min} of 0.14 was determined for a mixture of silty sand and gravel by [34]. The largest particle size is 13 mm meaning the sample diameter to largest particle diameter ratio is 15.4, which is large enough to obtain triaxial tests results

that are unaffected by particle size. Many standards require a minimum ratio of 6 in triaxial compression tests (e.g., ASTM D7187 [2]). When erosion is involved, a sample diameter to largest particle diameter ratio of 10 was found to minimize preferential flow between the sample boundary and a rigid mold the sample was contained in [17]. In this study, where a sample is contained in a flexible membrane under a confining pressure, meaning preferential flow will be less likely to arise than for the rigid mold, a ratio of 15.4 is adequate.

The sample formation procedure of [37] was used. It involved a specific reallocation of fine particles in the different compaction layers so a heterogeneous sample was formed. The subsequent erosion caused fine particle removal and relocation, through the layers, such that a homogenous PSD and e existed throughout the sample. When erosion was not to be imposed on a sample the conventional ‘undercompaction’ method [32] was used with each layer having the same PSD. With this method a variety of specific compaction energies were applied to different layers so that a homogeneous e was attained throughout the sample.

3 Test setup and procedure

To aid saturation, the samples were first flooded with carbon dioxide (CO₂) gas. The pressure of CO₂ at the base inlet was set to 15 kPa, while a hydrostatic confining pressure of 20 kPa was applied to sample boundaries. The inflow of CO₂ was allowed to occur for 30 min, replacing most of the air in the voids of the samples. Water was then passed through the samples, entering the base, driven by a constant water head and an average hydraulic gradient of 0.05. The water flow was sufficiently slow to minimize the filtration of fine particles in the samples, although a very small portion of fines near the top surface of samples were transported out, discussed later. The inlet and outlet valves were then closed and the pore pressure was slowly increased to 10 kPa. Prior to consolidation, erosion and triaxial testing, the back-pressure saturation was imposed until a B value of at least 0.92 was measured. The saturation phase lasted approximately 72 h, continuing until there was no further increase in the B value. Although the widely accepted criterion for saturation in a triaxial test is a B value greater than 0.95, a B value of 0.92, for mixtures of cohesionless silt, sand and gravel, and with void ratios around 0.25 to 0.4 like those here, indicates that saturation is sufficiently complete for drained tests to be conducted [31]. The back pressure and confining pressure were then reduced to 10 kPa and 20 kPa, respectively.

The samples were then consolidated. This involved gradually increasing the confining pressure to the desired value, slowly (2 kPa per minute) to avoid potential soil particle migration. During consolidation the pore volume was recorded every minute. After consolidation the samples were ready for erosion tests.

The erosion process used to create homogenous samples involved sequences of downward and upward water movements through the samples using a hydraulic gradient of 3.1. The constant head tank imposed a pore water pressure of 8.2 kPa, where water entered the samples. The outlet pressure was maintained at atmosphere pressure. This caused a slight gradient of effective stress to exist across the samples during erosion. After erosion the B value was checked. Saturation was repeated if the B value was smaller than 0.92.

The samples' homogeneities were then confirmed with examples detailed here. The three samples, denoted as GG27HOM, GG23HOM and GG32HOM, formed by the new sample formation procedure of [37], were subjected to $8 \times 10^{-3} \text{ m}^3$, $24 \times 10^{-3} \text{ m}^3$ or $48 \times 10^{-3} \text{ m}^3$ of seepage erosion, respectively. The seepage direction was reversed after every $8 \times 10^{-3} \text{ m}^3$ of water passed through a sample. For example, a total seepage volume of $48 \times 10^{-3} \text{ m}^3$ meant that six upward or downward seepage erosion stages

were applied, each being $8 \times 10^{-3} \text{ m}^3$. The pre-erosion and pre-consolidation dry densities were about 2.08 Mg/m³, corresponding to a relative density ($D_r = (e_{\max} - e)/(e_{\max} - e_{\min})$) of 50% and $e = 0.32$. For comparison another three samples, denoted GG24HET, GG15HET and GG13HET, formed by the conventional 'undercompaction' method, were subjected to $8 \times 10^{-3} \text{ m}^3$, $24 \times 10^{-3} \text{ m}^3$ or $48 \times 10^{-3} \text{ m}^3$ of unidirectional seepage and erosion, respectively. These were not expected to be homogenous. A 50 kPa confining pressure was applied for all cases. Post-erosion, the PSDs along the sample lengths were determined, as shown in Fig. 3. Samples prepared by the new sample formation procedure had more homogeneous post-erosion PSDs along their lengths (as shown in Fig. 3b, d and f) compared to those formed by the more conventional approach (Fig. 3a, c and e). Visual and quantitative comparisons confirmed this. The homogeneity variances, defined as the squared deviation of fine contents loss relative to the average fine contents loss, were 5.22, 23.81 and 24.31 for GG24HET, GG15HET and GG13HET, respectively, much larger than 0.38, 1.68 and 2.63 for GG27HOM, GG23HOM and GG32HOM, respectively. Similarly, the homogeneity variances for e were 0.000984, 0.00527 and 0.00604 for GG24HET, GG15HET and GG13HET, respectively, much larger than 0.000072, 0.000359 and 0.000641 for GG27HOM, GG23HOM and GG32HOM, respectively.

The seepage water which exited the samples was collected and the times required to reach target volumes were recorded so that the rates of discharge could be determined. Sample settlement and volumetric change were also determined at the end of each erosion stage. There was a pause of one minute between each erosion stage.

After erosion the pore pressure was increased to 210 kPa, the confining pressures were increased to 260, 310 or 410 kPa, corresponding to effective confining stresses of 50, 100 or 200 kPa, respectively. Drained triaxial compression tests were then conducted using an axial displacement rate of 0.2 mm/min.

The general characteristics of the erosion process were also studied, during which it was not intended to attain homogenous samples. Hydraulic gradients of 3.1 and 8 were used. The constant head tank imposed a pore water pressure of 20 kPa for a hydraulic gradient of 8. Again the water pressure was 0 kPa, where it exited a sample. A range of seepage sequences, involving unidirectional seepage as well as stages of upward and downward seepage, were applied. Again seepage water was collected and sample displacements and volume changes were recorded.

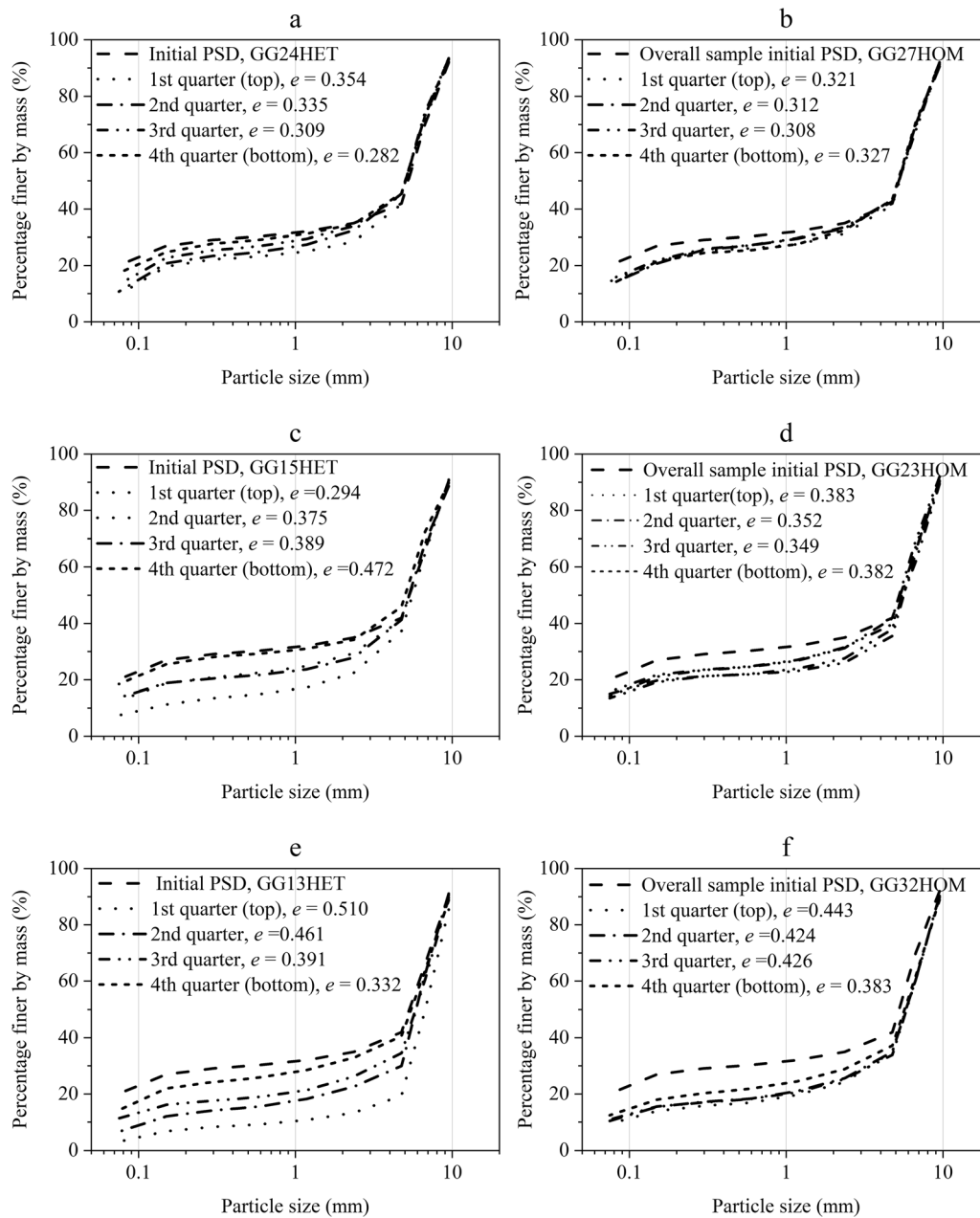


Fig. 3 Evaluation of the homogeneity of post-erosion particle size distribution (PSD). **a, c and e:** PSD and post-erosion PSD of control samples, where a conventional sample formation method was used; **b, d and f:** overall initial PSD and post-erosion PSD of samples, where Li et al. [37]'s sample formation procedure is used

4 Results and discussion of the erosion tests and triaxial tests

For a soil to experience internal erosion two general physical conditions must be satisfied. It must be possible for the flowing water to release particles from the mass of soil, and for the released particles to be carried along with the seepage. The PSD is important as well. The coarser fraction of the distribution is implicitly correlated with the range of pore (aperture) sizes through which finer eroded

particles must pass. The distribution of sizes in the finer fraction influences which of the finer particles will be carried through the soil. Also, the mass ratio of the finer fraction to coarser fraction has a significant influence on whether fines contribute to the load carrying skeleton of the soil or just fill the voids around a load carrying skeleton made of coarser particles [51, 57, 60]. Skempton and Brogan [60] proposed that the critical fine fraction, it being the minimum fraction required for the finer particles to play a major role in load transfer, was generally around 24–

29%, depending on D_r . They also proposed that fine fractions larger than 35% would cause the fine particles to separate the coarser particles from one another and the material to be ‘overfilled’ and thus internally stable. There are some obvious problems linked with the segmentation of the PSD in to coarser and finer fractions. Where does the coarser fraction end and where does the finer fraction begin and what’s the mass ratio of the coarse and the fine fractions? When the soil is truly gap-graded, like that considered here, then the answers to these questions may be uncontroversial. For gap-graded and other soils, there are various generally accepted criteria (listed in Table 1) which link the erosion susceptibility to the PSD.

Also, the soil can exist at any e (or D_r) between its maximum and minimum values. The load transfer when the finer fraction is between 24 and 35%, especially how the load is shared between coarser and finer fractions, is highly sensitive to D_r . An increase in D_r enhances the loads carried by the finer fraction, and therefore, increases the resistance to erosion initiation and internal stability [58]. The k of the soil, and thus the flow rate and hydraulic velocity, also vary strongly with e . The higher the e the higher the rate of flow, velocity and more rapid the erosion. As the flow velocity increases so does the shear stress that the water imposes on a potentially erodible soil particle. A particle Reynold’s number, $R_e = \rho\omega d/\mu$, may relate to the potential of a particle to detach and be carried through the soil, where ρ = water density, d = particle diameter, μ = water dynamic viscosity and ω = flow velocity.

The ease with which particles can be detached may also depend on the current stress state and the directions of principal stresses relative to the direction of flow. A high mobilized friction means the stress state is highly anisotropic. The largest of the particle contact forces are aligned,

predominantly, in the direction of the major principal stress. A flow normal to that direction may be more likely to detach particles as the resistance (compressive reaction forces) provided by neighboring particles is lesser than when the flow occurs in the same direction as the major principal stress. When the stress states are near isotropic during erosion, as is the case here, the resistance to erosion provided by neighboring particles will be proportional to the applied stress and D_r .

Evidence in support of these general premises, and the mechanical changes to the soil’s state and mechanical properties which result from erosion, are explored in more detail below. The observed general erosion characteristics are detailed first. Then the erosion-induced stress–strain behaviors, and state changes, are detailed.

4.1 Erosion characteristics

A range of soil properties and erosion-related phenomena have been measured by others in studies of this type including the change in PSD [28, 57], mass loss [7, 27], the change in permeability [27, 33, 59], the flow rate and discharge velocity [35, 60] and the possible rearrangement of the soil structure [30].

Here, the quantities measured included the cumulative eroded mass with time, the volume of seepage water with time, as well as axial strain and volumetric strain.

The flow rate is used here, as an indicator of the progress of erosion. It is not practically possible to determine the hydraulic velocity in a reliable way. The flow rate for each erosion stage is defined as:

$$Q = \frac{V}{t} \quad (1)$$

Table 1 The evaluation of the mixture’s erodibility using various methods

Criteria	Condition for the mixture to be internally stable	Assessment
Sherman [57]	$C_u < 20$	Unstable
Istomina [23]	$C_u \leq 20$	Unstable
Lubochkov [39]	$(\Delta S1/\Delta S2)/F \leq 1$	Unstable
Kézdi [30]	$(d_{15c}/d_{85f})_{\max} \leq 4$	Unstable
Kenney and Lau [28, 29]	$(H/F)_{\min} > 1 (0 < F < 0.3)$	Unstable
Burenkova [8]	$0.761\log(h'') + 1 < h_0 < 1.861\log(h'') + 1$	Unstable
Wan and Fell [64]	$P = \frac{\exp(Z)}{[1-\exp(Z)]}$ $Z = 2.378\log(h'') - 3.648h'$	$P = 95\%$ probability that in will be unstable

Notations: d = particle size (diameter), d_x =the particle size that corresponds to $x\%$ of the soil passing by weight, $C_u=d_{60}/d_{10}$ (coefficient of uniformity), $h'=d_{90}/d_{60}$, $h''=d_{90}/d_{15}$, $\Delta S1$ =difference between weights of particles of size d_{n-1} and d_n , $\Delta S2$ = difference between weights of particles of size d_n and d_{n+1} , F =fraction by weight of a soil which is finer than size d_n , d_{15c} and d_{85f} are from the soil being separated into a coarse and a fine fractions and each fraction is rescaled

where V is the discharge volume and t is time for each erosion stage. The mass of eroded soil in the seepage water was also determined.

The average permeability (k_{ave}) for each erosion stage may be defined as:

$$k_{ave} = \frac{Q}{iA} \quad (2)$$

where A is the cross-sectional area of the test sample and i is the hydraulic gradient.

The cumulative eroded soil mass is another indicator that reflects the initiation and development of internal erosion. Generally, the cumulative eroded soil mass increases dramatically in the early stages once the erosion initiates, then gradually and eventually approaches a constant [7, 27, 37, 49, 59].

The initial conditions of the samples tested, as well as the hydraulic gradients and seepage sequences applied to cause erosion, are summarized in Table 2. The soil samples used in these particular erosion tests were formed by the conventional sample formation procedure meaning they had a homogeneous density and PSD throughout before erosion.

4.1.1 The influence of initial relative density

Three samples GG03, GG04 and GG08, with initial D_r of about 30%, 50% and 70%, respectively, were prepared. A hydraulic gradient 8 and a confining pressure of 50 kPa were applied as erosion took place in these particular tests. Other hydraulic gradients and confining stresses were applied in other erosion tests, detailed later. Each sample had a total of $96 \times 10^{-3} \text{ m}^3$ of water passed through them, through six upward–downward seepage cycles. The variations of flow rate and cumulative eroded soil mass are plotted in Fig. 4. Each symbol, either square, triangle or circle, indicates the end of an upward or downward part of a cycle involving $8 \times 10^{-3} \text{ m}^3$ of seepage.

The flow rate through each sample increased then became stable. The flow rate for the initial D_r of 30% was the highest and for the initial D_r of 70% was lowest. The different flow rates indicate that there is more energy dissipated (or head lost) in a dense soil, in agreement with [63].

The flow rate for the sample with an initial relative density of 70% increased slightly for the first 2000 s, then entered a period of rapid increase, then became stable. A less pronounced but noticeable increase in the flow rates occurred in the looser samples as well, at 420 s and 280 s for 50% and 30% relative densities, respectively. It takes time for internal erosion to initiate and fully develop. The changing flow rates can be attributed to the particle removals which cause increases to the average permeabilities of the samples.

The cumulative eroded soil mass increased with time until a stable value was approached. The first $8 \times 10^{-3} \text{ m}^3$ of seepage water transported the largest amount of the eroded soil mass when compared to subsequent seepage stages. The mass of eroded soil gradually decreased for each stage as the number of stages increased.

Also, the cumulative eroded soil mass increased with the decrease in initial relative density. This is consistent with the flow rate increasing with the decrease in relative density.

4.1.2 The influence of hydraulic gradient

The magnitude of the hydraulic gradient influences the initiation and development of internal erosion. Some researchers identified a critical value of the hydraulic gradient, it being the lowest value required for internal erosion to initiate, by starting with very small values and then gradually increasing them until internal erosion was observed [45, 59, 60, 63]. Others monitored the evolution of the hydraulic gradient within a soil during erosion under a constant water head or flow rate [27, 45].

Table 2 A summary of sample conditions and erosion procedure

Soil sample	Targeted initial relative density (after compaction)	Confining stress (kPa)	Actual relative density after consolidation (before erosion)	Actual void ratio after consolidation (before erosion)	Hydraulic gradient	Seepage passing through (10^{-3} m^3)
GG03	30%	50	34.2%	0.383	8	12×8
GG04	50%	50	56.2%	0.288	8	12×8
GG08	70%	50	71.6%	0.222	8	12×8
GG11	50%	50	56%	0.289	8	3×15
GG17	50%	100	60%	0.272	8	3×15
GG20	50%	200	61%	0.268	8	3×15
GG28	50%	50	56.1%	0.288	3.1	12×8

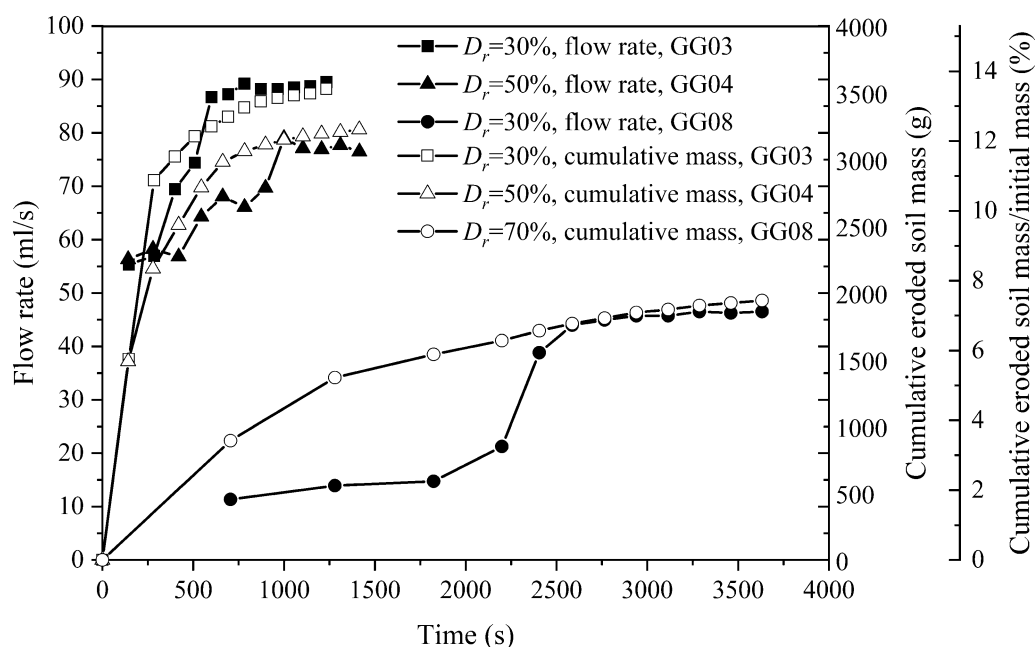


Fig. 4 Flow rate and cumulative eroded soil mass with time considering the effects of initial relative density

Here, two hydraulic gradients, 3.1 and 8, were applied to soil samples GG04 and GG28, respectively, having the same confining stresses (50 kPa) and initial D_r (50%). Although hydraulic gradients in the bulk of a dam structure are typically less than 0.5, hydraulic gradients of 2 or larger frequently exist in localized areas and are sufficient to trigger internal erosion [7, 13, 64]. The hydraulic gradient that initiates the internal erosion of a gap-graded soil is usually small [60], and may correspond to a very slow

erosion process, while the hydraulic gradient that induces a significant loss of fine particles and erosion may be much larger [45]. For example, Chang and Zhang [13] found that in their triaxial erosion tests on a gap-graded soil, a hydraulic gradient of 1.2 was sufficient for initiation, while a sudden increase in erosion rate was observed when the hydraulic gradient increased to 3.15.

In this study, trial tests with different hydraulic gradients were conducted and it was found that 3.1 was sufficient to

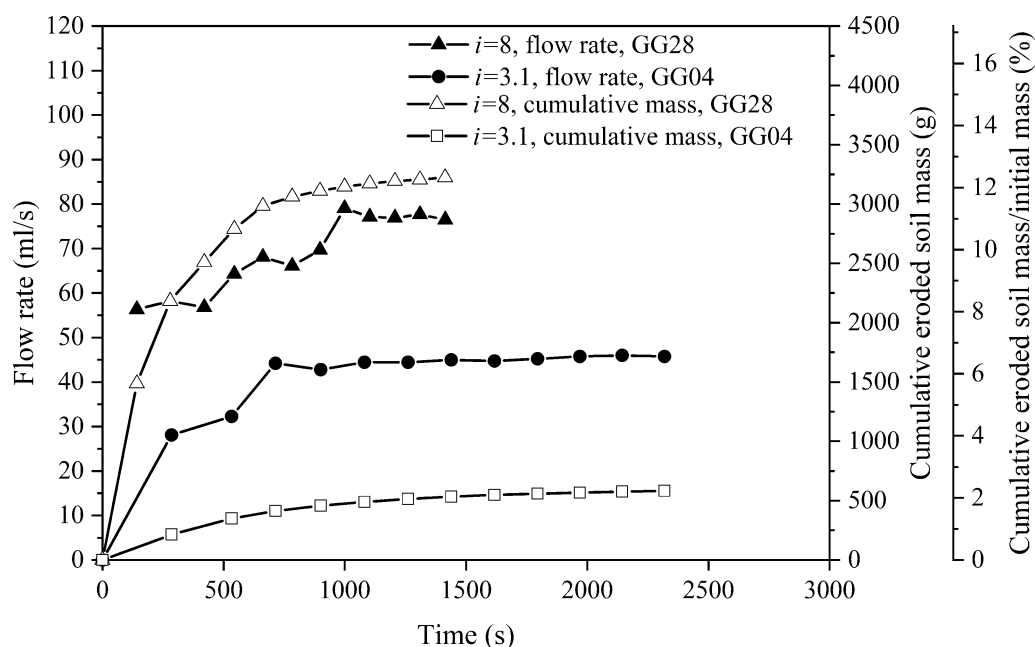


Fig. 5 Flow rate and cumulative eroded soil mass with time considering the effects of initial hydraulic gradient

initiate the erosion and induce a significant amounts of fines loss within a relatively short time (from dozens of seconds up to 1 h). The erosion under a hydraulic gradient of 8 was compared to that for 3.1. A hydraulic gradient of 8 was also used by [13, 64], representing an extreme condition that soils at filters or transition zones of a dam may experience. The results (Fig. 5) indicate that the flow rate under a hydraulic gradient of 8 was larger at all stages compared to that under a hydraulic gradient of 3.1. The total time consumed to cause passage of $12 \times 8 \times 10^{-3} \text{ m}^3$ of seepage for a hydraulic gradient of 8 was much less than that for a hydraulic gradient of 3.1.

A hydraulic gradient of 8 caused significantly greater fine particle losses at the beginning of erosion (Fig. 5). This is consistent with [59]'s conclusion that the cumulative eroded soil mass increases with hydraulic gradient. The higher hydraulic gradient induces a higher hydraulic shear stress and a lower effective stress at constant confining stress [7]. When seepage passes through the soil skeleton formed by coarse particles, in which fine particles fill the pore spaces around coarse particles, the fine particles are more easily removed as hydraulic shear stress increases and the effective stress decreases.

4.1.3 The influence of effective confining stress

A particle's resistance to erosion is provided by neighboring particles and is proportional to the magnitude of the contact forces and confining stress, which is supported by [7] and [13]'s experimental observations that the increase

in confining stress increases the internal erosion resistance of a soil.

Figure 6 shows the variations of flow rate and cumulative eroded soil mass with time for three tests. Each sample had an initial relative density of 50%, corresponding to $e = 0.32$. Each sample was subjected to a seepage of $45 \times 10^{-3} \text{ m}^3$ (through an upward-downward-upward seepage cycle, with $15 \times 10^{-3} \text{ m}^3$ passed through each stage of the cycle) under a hydraulic gradient of 8. The samples, denoted as GG11, GG17 and GG20, were consolidated under confining stresses of 50, 100 or 200 kPa, respectively. The erosion and consolidation caused the D_r to increase to 56%, 60% and 61%, and the e to reduce to 0.29, 0.27 and 0.26, respectively.

The flow rates increased in successive stages of the seepage. The sample with the lowest confining stress (i.e., with the largest e) exhibited the largest flow, whereas the sample with the largest confining stress (the smallest e) exhibited the smallest flow rate. Flow rate appears to increase with increasing e and decreasing D_r . The cumulative eroded soil mass was also affected by confining stress. The sample with 50 kPa confining stress exhibited a near uniform and rapid increase in eroded soil mass (about 1500 g in 500 s) from the commencement of seepage. The samples with 100 and 200 kPa confining stresses exhibited rapid increases but starting at a significant time after the onset of seepage. Specifically, for the sample with 100 kPa confining stress, the eroded soil mass was about 10 g in first 850 s, followed by 144 g in the subsequent 280 s, and then 850 g in the final 242 s. For the sample with 200 kPa

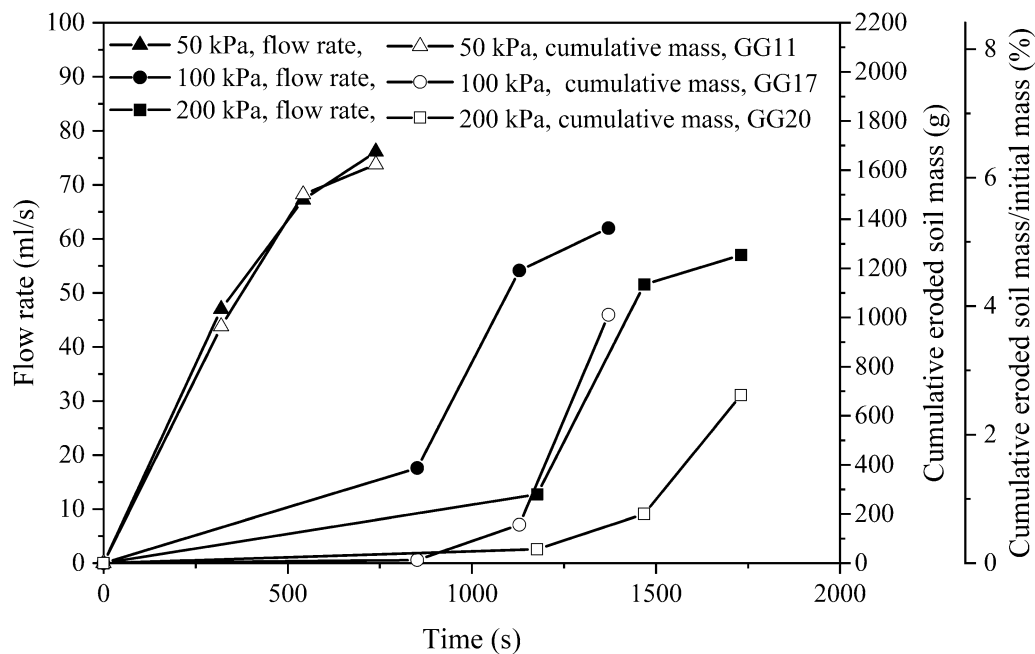


Fig. 6 The variation of flow rate and cumulative eroded soil mass with time under different confining stresses

confining stress, the eroded soil mass was 56 g in first 1200 s, followed by 150 g in the subsequent 300 s and 485 g in the final 260 s. It is evident that the initiation of internal erosion occurred later as the confining stress was increased. Once the erosion initiated, its development tended to accelerate, for a period of time, in the samples with the higher confining stresses.

4.1.4 The impacts of reversing the seepage direction

Reversals of the seepage, changing between vertical upward and downward directions, occurred when forming the eroded samples with homogeneous post-erosion PSDs. The samples had heterogeneous PSDs prior to the erosion. There are obvious differences between this type of erosion and what happens inside embankment dams. In embankment dams the seepage is mostly unidirectional, may occur off the vertical, and initially the soil is mostly homogeneous in its PSD. Moffat and Fannin [44] showed that the onset of instability in rigid wall permeameter is independent of whether an upward or downward seepage was applied. However, the way and rate by which fine particles are detached and transported, and the formation of a stable particle and pore size distributions, will likely differ for the two scenarios.

There are significant benefits to having homogenous PSDs that were formed using a reversing seepage. As already mentioned, homogeneity makes it much easier to relate observed stress–strain behaviors and strengths to the soil's state and amount of erosion so that constitutive models can be developed and safety assessments can be made. Also, reversing the seepage imposes alternating positive and negative hydraulic gradients as a sample is

formed. When unidirectional seepage is used and the hydraulic gradient is fixed a nonuniform effective stress exists along a sample's length, meaning the sample does not consolidate homogeneously [45].

Also, the eroded mass loss may be quite different for upward and downward seepage, due to gravity [45]. Gravity will have most influence when the weight of a single particle is greater than the driving force by seepage. Here, the particles in the eroded finer fraction were mostly silt sized, with 50% smaller than 0.04 mm. The fines remained dispersed in the seepage water. Their settlement in still water takes more than 24 h. It is reasonable to assume that the weights of the silt particles are smaller than the driving forces by seepage. Reversing the seepage tends to average out any effects of this phenomenon.

Figure 7 plots the eroded mass loss at the end of each erosion stage and the cumulative eroded mass for downward or upward stages for samples with initial D_r of 30%, 50% and 70%, together with the duration for each erosion stage or the overall duration for each seepage direction. It is clear that the eroded mass loss per stage decreases with the development of erosion, and that there are no major influences of seepage direction reversals in the later stages. The mass loss due to downward seepage is, in general, slightly larger than that during upward seepage although that is because the first stage removed the largest mass of soil and happen to be in a downward direction.

The durations in Fig. 7a, b, of each stage and overall for all stages, appear to be influenced by D_r . The durations were significantly longer for D_r of 70% than 30% and 50%.

It is not expected that the reversals of seepage direction significantly altered the force chains through a sample nor altered the forces acting on the finer and potentially

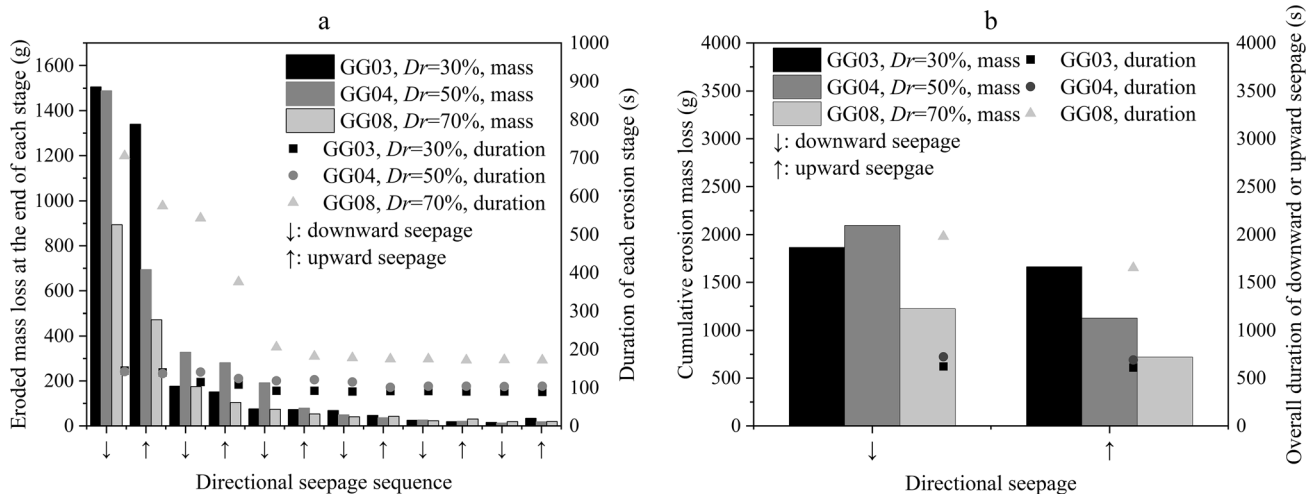


Fig. 7 The effect of directional seepage sequence on eroded soil mass and duration for samples with different initial relative density: **a** Eroded mass loss and duration at the end of each erosion stage plotted against directional seepage sequence; **b** Total erosion mass loss for downward and upward seepage directions

Table 3 Comparison between the cumulative soil mass and the total soil mass

Soil sample	Cumulative eroded soil mass at the end of erosion (g)	Mass of soil retained in drainage system (g)	Mass loss during saturation (g) (% of mass loss during saturation over total mass loss)	Total soil mass loss (g)	The ratio between cumulative eroded soil mass and total soil mass loss
GG03	3528.8	489.1	40.5 (0.96%)	4199.8	0.840
GG04	3224.2	422.1	55.3 (1.49%)	3701.6	0.871
GG08	1944.3	378.4	22.8 (0.9%)	2345.5	0.829
GG11	1623.0	211.5	23.7 (1.2%)	1858.2	0.873
GG17	1010.9	177.1	8.7 (0.73%)	1196.7	0.845
GG20	684.6	262.4	15.2 (1.5%)	962.2	0.710
GG28	783.0	341.1	71.4 (5.96%)	1197.5	0.654

erodible particles. According to [38], for soil with 25–30% fines, similar to that used in this study, the strong forces acting on the fine particles were negligible.

4.1.5 The limitation of using the cumulative eroded soil mass as an indicator of erosion

A limitation of using the cumulative eroded soil mass as an indicator of internal erosion, when measured using the seepage water which exits the samples, is that it may underestimate the true mass losses. A comparison of the cumulative eroded soil mass and the total eroded soil mass is given in Table 3.

The total mass loss includes that deposited and remaining in the drainage lines, in the conical cavities in the equipment at each end of the sample, as well as that contained in the seepage water. The mass of particles in the drainage lines and conical cavities was as large as 29% of the total mass loss in some cases. Mass losses also occurred during saturation, and generally ranged from 0.73 to 1.5% (except for test GG28 where it was 5.96% due to the much larger volume of water that had to be passed through that sample to saturate it).

4.1.6 Other observations

The vertical settlement was measured by reading the vertical differences between where a horizontal laser mark was projected on the top cap of the soil sample, before and after an erosion test. Of all the erosion tests only a few exhibited a vertical settlement, being less than 1 mm each time. Therefore, the vertical settlement was assumed negligible in subsequent calculations of volume and height.

Samples generally reduced in volume as erosion occurred but by very small amounts. The volumetric strains at the end of internal erosion were generally less than about 0.002, i.e., negligible. The internal erosion process is then

consistent with that known as suffusion, i.e., it occurs without a significant volume change [18].

Turbidity may be used to describe, the degree to which the exiting seepage water has lost its transparency due to the presence of suspended particles. In a series of erosion tests [22], found that there is a linear relationship between the concentration of particles in the seepage water and the turbidity. Here, it was found that, when a large number of fines were suspended in the seepage water, the turbidity meter was unreliable. Typically, the seepage water was (nearly) transparent for the first few seconds, then erosion initiated and the effluent color changed to cream/brown. As seepage continued and erosion gradually reduced a fade in the color was observed, with the seepage water becoming nearly transparent, indicating the end of erosion.

4.1.7 Relationship to published erosion criteria

The susceptibility of this particular gap-graded soil to internal erosion was evaluated using various criterion [8, 23, 28–30, 57, 64], as shown in Table 1, each indicating internal instability. Each criterion incorporates particle size information. Their application, and the evaluation of the erodibility of the soil, have been detailed quantitatively by [36]. There is an inherent assumption that the soil has a homogeneous PSD and e for a certain criterion to be applicable. Suffusion is usually accompanied by self-filtration [7, 21] and there may be cases where, due to localized heterogeneity, self-filtering occurs preventing erosion from taking place. If a sample was taken, capturing both coarse and fine sections, some criterion may give false indications of erosion susceptibility.

Alternate criterion may also incorporate information related a soil's e or pore size distribution. Some advances have already been made [7, 25, 40] although are very empirical thus may have limited applicability. Theories which relate e to pore and particle sizes in unique ways have been developed for soils with fractal PSDs [53] and

soils with only one particle size [61]. There is a need to bridge these two theories to find applicability to the myriad of other possible PSDs.

4.2 Stress–strain behavior changes and state changes due to internal erosion

Conventional triaxial $p' - q$ notations are used here, when presenting the triaxial test results, including: mean effective stress $p' = (\sigma'_1 + 2\sigma'_3)/3$; deviator stress $q = \sigma'_1 - \sigma'_3$; volumetric strain $\varepsilon_p = \varepsilon_1 + 2\varepsilon_3$; shear (deviator) strain $\varepsilon_q = 2(\varepsilon_1 - \varepsilon_3)/3$, where σ'_1 and σ'_3 are principal effective stresses and ε_1 and ε_3 are the conjugate principal strains. A superscript dash denotes the invariant to be effective, subscripts 1 and 3 denote the major (axial) and minor (radial) components, respectively. Compressive stresses and strains are assumed to be positive and volumetric strain is given by:

$$\varepsilon_p = -\ln\left(\frac{v}{v_0}\right) \quad (3)$$

which has the incremental form:

$$\delta\varepsilon_p = \frac{-\delta v}{v} \quad (4)$$

where v is the current specific volume ($v = 1 + e$) and v_0 is the specific volume when strains are zero. Area corrections were also made in the usual way.

Reference is also given to aspects of critical state soil mechanics [46]. A soil sheared to a large shear strain will

approach a critical state, where it distorts (shears) continuously without changes in volume or the imposed effective stresses. The combinations of p' , q and v at the critical state form a unique line in the three-dimensional $v \sim p' \sim q$ space. In drained triaxial compression tests localized shear bands often occur before a critical state is reached, mainly due to slight heterogeneities in the samples and/or friction at the sample boundaries, requiring some judgment to be applied when interpreting the results [15, 24].

The properties of the samples, seepage volumes used to cause erosion, and key indicators of strength are summarized in Table 4.

4.2.1 Stress–strain behaviors and strengths

GG27HOM and GG29HOM were prepared, eroded and tested under identical conditions and the good agreement between the results confirms the repeatability of the procedures followed, as shown in Fig. 8. Figure 9 plots the full stress–strain curves together with the volumetric strain curves for the set of tests GG14, GG23HOM, GG27HOM and GG32HOM, each having an effective confining stress of 50 kPa. Figure 10 plots the full stress–strain curves together with the volumetric strain curves for the set of tests GG18, GG39HOM, GG38HOM and GG31HOM, each having an effective confining stress of 100 kPa. Figure 11 plots the full stress–strain curves together with the volumetric strain curves for the set of tests GG16, GG36HOM and GG37HOM, each having an effective confining stress of 200 kPa. Figure 12 plots the friction

Table 4 Summary of triaxial compression test conditions and results under the effective confining stress of 50, 100 and 200 kPa

Sample	Effective confining stress (kPa)	Seepage passing through (10^{-3} m^3)	Mass loss during erosion (%)	Void ratio before shearing	Peak strength (kPa)	Friction angle at peak ($^\circ$)	Friction angle at large strain ($^\circ$)	Angle of dilation ($^\circ$)
GG14	50	0	0	0.254	386	52.6	43.8	19.2
GG27HOM	50	1 × 8	3.90	0.316	358	51.4	43.3	17.2
GG29HOM	50	1 × 8	4.20	0.314	356	51.3	42.6	18.2
GG23HOM	50	3 × 8	6.32	0.354	328	50.0	42.6	15.2
GG32HOM	50	6 × 8	10.08	0.418	309	49.1	42	14.3
GG18	100	0	0	0.253	583.1	48.3	44.1	8.7
GG39HOM	100	1 × 8	3.70	0.313	555.2	47.1	43.4	7.4
GG38HOM	100	3 × 8	6.05	0.344	537.2	46.7	42.9	7.5
GG31HOM	100	6 × 8	8.90	0.387	494.5	45.2	42.5	5.18
GG16	200	0	0	0.250	852.5		42.7	
GG36HOM	200	3 × 8	5.85	0.339	827.6		42.2	
GG37HOM	200	6 × 8	9.30	0.393	816.9		42.5	

The friction angle at peak for GG16, GG36HOM and GG37HOM are not presented as the stress–strain curve are strain hardening and no evident peaks are shown, and these three show contractive responses in volume change, while others show dilative responses. The angle of dilation follows the definition of [46]

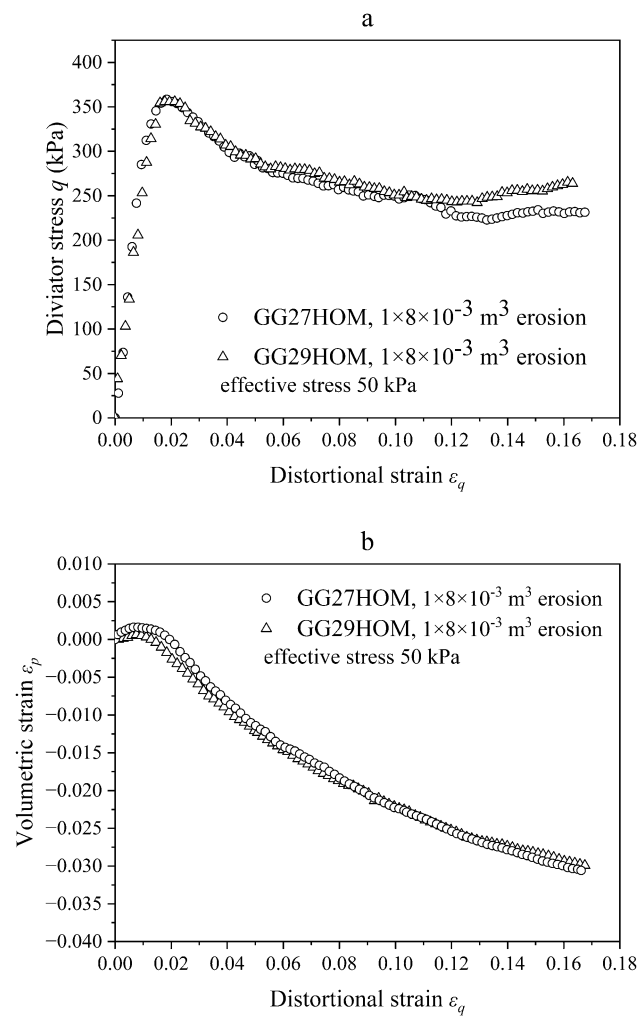


Fig. 8 Drained compression repeatability tests on samples GG27HOM and GG29HOM under effective stress of 50 kPa. **a** Stress–strain relationships. **b** Volumetric strain and shear strain relationships

angles mobilized at peak strength conditions, and large shear strains, against the erosion-induced mass loss.

The friction angle at the peak condition (Fig. 12) generally decreased with increased amounts of erosion, corresponding to increased e as well. There is also an effective confining stress dependency, as discussed above. The peak friction angle reductions, following increases of erosion and fine particle removal, are in agreement with [12, 27, 48].

The friction angle at large shear strain is generally unaffected by the amount of erosion or effective confining stress (Fig. 12), indicating that the critical state friction angle and critical friction ratio M can be treated as constants, as often done in soil mechanics, irrespective of the amount of erosion. Yang and Wei [67] and Yang and Luo [68] conducted triaxial tests on mixtures of angular/round fines and uniform coarse sand. They observed that adding

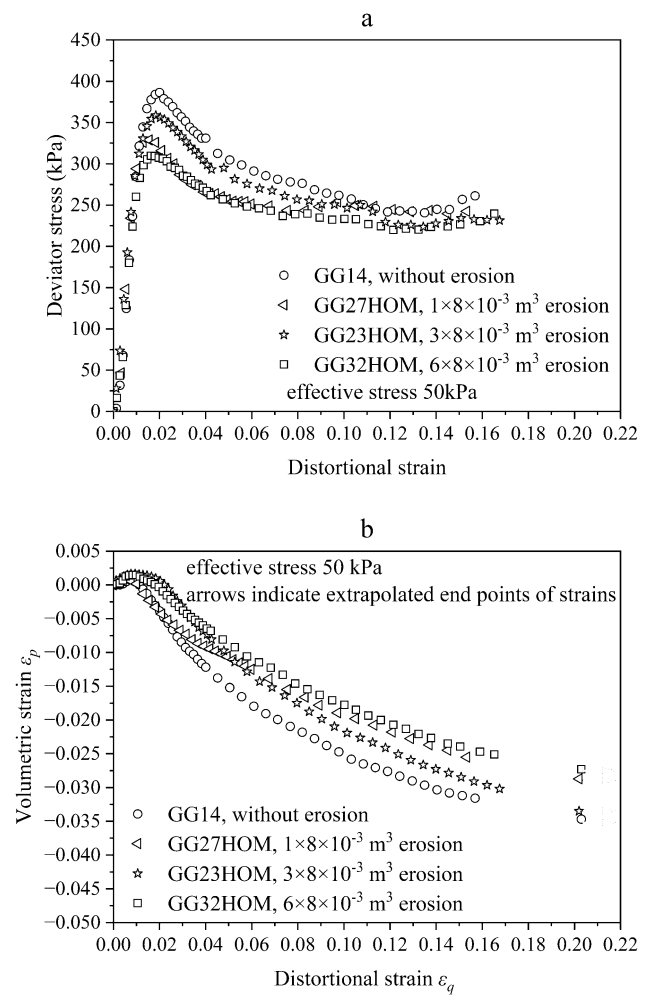


Fig. 9 Drained compression tests on samples (GG14, GG23HOM, GG27HOM and GG32HOM) subjected to different amounts of internal erosion under effective stress of 50 kPa. **a** Stress–strain relationships. **b** Volumetric strain and shear strain relationships

angular fines, like crushed silica, to the base sand resulted in a slight increase in the critical state friction angle (from 31.3° to 31.9°). That increase was observed when the fines content was increased from 0 to 15%. Conversely, when round fines, like glass beads, were added and the fines content was increased from 0 to 10%, the critical state friction angle decreased from 31.3° to 27.83° . Their investigation showed that in influencing the value of M , angular fines (such as the silica used in this study) have a less significant impact than round fines. Furthermore, Yang and Luo [69] pointed out that when the influence of particle shape was removed the critical state friction angle is not affected by the PSD. McDougall et al. [42] observed an increase in M due to particle loss in triaxial compression tests on sand–salt mixtures, but the tests involved salt particles crushing causing an increasing fines content during compression, so may not be directly relevant to the observations made here. For angular fines, treating M as a

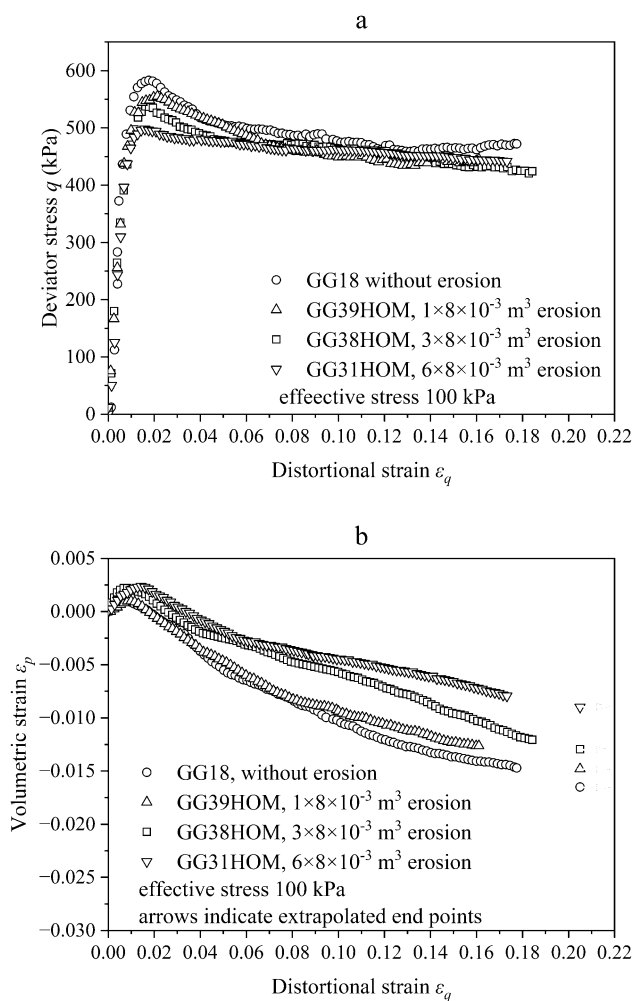


Fig. 10 Drained compression tests on samples (GG18, GG39HOM, GG38HOM and GG31HOM) subjected to different amounts of internal erosion under effective stress of 100 kPa. **a** Stress–strain relationships. **b** Volumetric strain and shear strain relationships

constant will simplify the development of constitutive models for soils subjected to erosion, especially since M has a key role in most models.

Samples subjected to 50 and 100 kPa confining stresses exhibited dilative responses, shown in Fig. 9b and Fig. 10b. Samples subjected to 200 kPa confining stresses exhibited contractive responses, shown in Fig. 11b.

In general the larger confining stress caused samples to exhibit a strain hardening behavior (Fig. 11a). Sample GG16, which had not undergone internal erosion, exhibited a slight peak in the mobilized strength at small shear strains (less than 0.02). At large strains, there were no noticeable differences in strengths between the samples, whatever the amount of erosion.

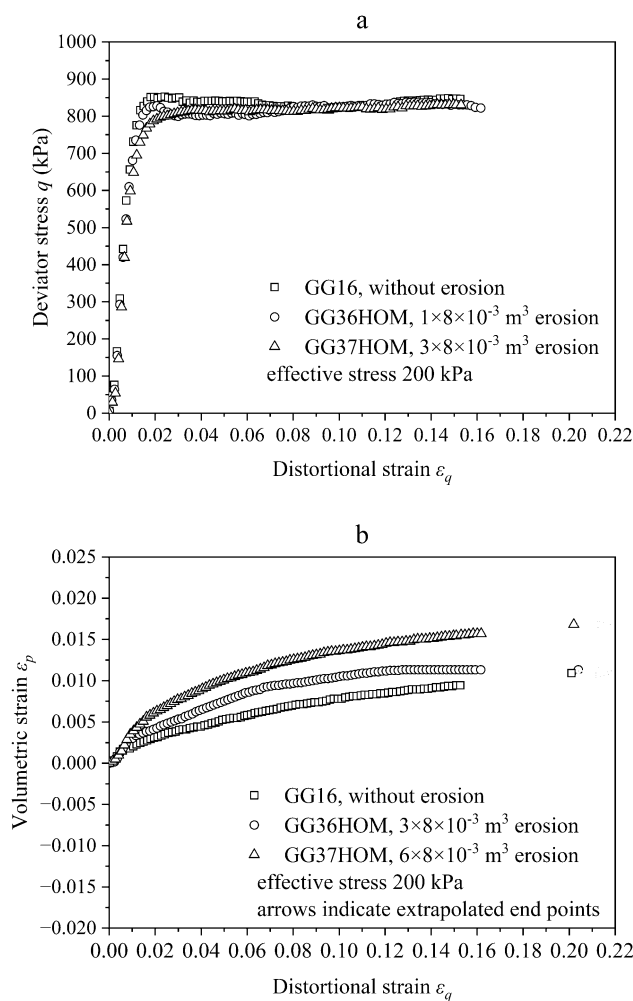


Fig. 11 Drained compression tests on samples (GG16, GG36HOM and GG37HOM) subjected to different amounts of internal erosion under effective stress of 200 kPa. **a** Stress–strain relationships. **b** Volumetric strain and shear strain relationships

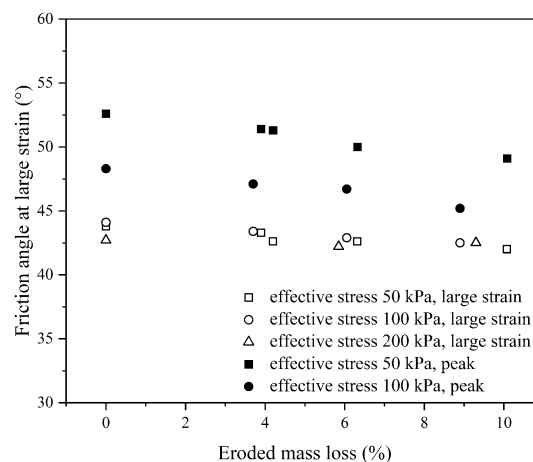


Fig. 12 Friction angles at peak strength conditions and large strains plotted against eroded mass loss

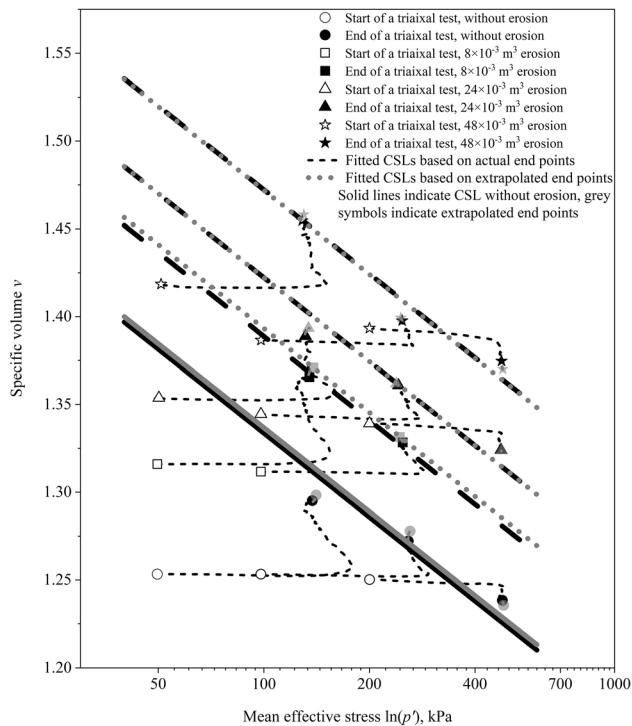


Fig. 13 Critical state of selected testing samples subjected to varying amounts of internal erosion on compression plane. The average mass losses were 3.9%, 6.1% and 9.4% for seepage volumes of 8, 24 and $48 \times 10^{-3} \text{ m}^3$

4.2.2 Evolution of state due to different amounts of internal erosion

Soil samples attained different PSDs and e once they had been subjected to different amounts of erosion and consolidation.

One dominant effect of a changing PSD, either by internal erosion or particle crushing, is a relocation of the

critical state line (CSL) in the compression ($v \sim \ln(p')$) plane [48, 50, 62, 67, 68]. Over a limited stress range (40–600 kPa) it is reasonable to use a straight line to define the CSL:

$$v_{cs} = \Gamma - \lambda \ln(p') \quad (5)$$

so a relocation corresponds to a change to the intercept with $p' = 1 \text{ kPa}$ (Γ) and/or slope (λ). However, other types of critical state line definitions, such as a curved line [9, 67, 68], could also be used and may be more suitable when larger stress ranges are involved.

Differing experimental observations, and modeling approaches, around how a fines content change affects the location of the CSL have been reported in the literature. Some indicate that a change in fines content causes a change to λ as well as Γ [6, 16, 74]. Others indicate the λ change is minor, and therefore, can be ignored such that the CSL relocation is controlled only by Γ [11, 48, 72, 73]. The latter was found to be reasonably consistent with the CSL data extracted from the experiments in this study. Besides, assuming λ as a constant makes modeling the mechanical consequences of internal erosion in the framework of critical state soil mechanics simpler.

The stress paths in the compression plane are shown in Fig. 13. Small extrapolations (also adopted by [1, 5]) were necessary to identify the critical state when the samples approached it but did not reach it. Also shown are extrapolated end points for each test, noting that volumetric strains were changing slightly with increasing shear strains, although decelerating, at the ends of the triaxial tests. The extrapolated end points were determined by eye, accounting for the different rates of deceleration leading up to where the actual data ended. The CSLs, having a single slope λ but different Γ , are fitted to the end points of each extrapolated data set corresponding to a certain volume of

Table 5 A comparison of the changes in void ratio due to erosion and the upward movements of CSL

Seepage passing through (10^{-3} m^3)	Sample	Change in void ratio due to erosion	Average change in void ratio	Upward movement of CSL	Average grading state index
1 × 8	GG27HOM	0.061	0.061	0.0565	0.798
	GG39HOM	0.061			
3 × 8	GG23HOM	0.112	0.106	0.0855	0.693
	GG38HOM	0.105			
	GG36HOM	0.101			
6 × 8	GG32HOM	0.167	0.155	0.135	0.456
	GG31HOM	0.146			
	GG37HOM	0.152			

The listed grading state indices, which are averages for each particular seepage volume, were determined by assuming the particle size distribution without erosion is double-fractal. The particle size distribution for no erosion is also the reference distribution and corresponds to a grading state index of 1. The maximum and minimum particle sizes for the coarse fraction were $d_{c_max} = 11 \text{ mm}$ and $d_{c_min} = 0.13 \text{ mm}$ and the fractal dimension was $D_{s_c} = 1.62$. The maximum and minimum particle sizes for the fine fraction were $d_{f_max} = 0.13 \text{ mm}$ and $d_{f_min} = 0.001 \text{ mm}$ and the fractal dimension was $D_{s_f} = 2.35$

seepage water to cause the erosion. The fitting parameters are $\lambda = -0.069$ and $\Gamma = 1.654, 1.711, 1.740$ and 1.790 , for $0, 8, 24$ and $48 \times 10^{-3} \text{ m}^3$ of seepage, respectively. The coefficients of determination (R^2) for each of the fitted CSLs are $0.8403, 0.9998, 0.9350$ and 0.9576 , respectively, with an average R^2 of 0.9332 . The average mass losses were $3.9\%, 6.1\%$ and 9.4% for seepage volumes of $1, 8$ and $24 \times 10^{-3} \text{ m}^3$.

The solid line represents the CSL for the soil when it has not eroded. It can be seen that the CSL moves upwards with the increase in seepage volume and thus the amount of erosion, in accordance with the discrete element modeling results of [48] and [74]. This is partly due to the soil being sheared from progressively looser initial states and partly due to the changing PSD. Similarly, Yang and Wei [67] observed a downward movement of the critical state line as the fines content increased.

Changes to the state parameter (being the vertical distance between the current v and the v on the CSL at the same p') also occurred. After an amount of erosion the CSL moved upwards and the v (and e) increased. However, the increase in v (due to fines content loss) was greater than the vertical distance that the CSL moved, in agreement with the modeling results by [10]. The state parameter, therefore, increased with erosion (i.e., became less negative) causing the soil to be more contractive and exhibit a reduced peak strength (discussed above). The changes in e due to different amounts of seepage erosion and the movements of CSLs have been listed in Table 5. It is clear that the change in e is slightly greater than the upward movement for soil samples having undergone the same amount of internal erosion.

While these observations are in general agreement with those of [11], [11]'s results were obtained from samples which had heterogeneous post-erosion e and PSDs along their lengths. There is some uncertainty around how to define a representative e , PSD and state parameter for heterogeneous samples, making it difficult to interrelate the [11] measurements and state.

Also, the volumetric deformations of samples became more contractive at small shear strains with increasing amounts of erosion and increasing initial state parameters. Also, at large shear strains, the samples which had experienced erosion showed a reduced tendency for dilation compared to the samples which had not experienced internal erosion, consistent with the initial state parameter increases. The erosion caused the samples to become looser and thus tend to be more contractive at large shear strains, in agreement with [12].

McDougall et al. [41] observed changes resulting from dissolution-induced particle loss. Rousseau et al. [52] developed a e -dependent model to explain stress–strain

behavior alteration due to erosion. These studies focused only on the change in e but did not take account of the change in CSL or state parameter.

The CSL locations may be better presented as a function of a grading state index rather than the volume of seepage which passed through the soil to cause the erosion or mass loss. This will be explored by the authors in a future paper where a full constitutive model, incorporating the grading state index, will be presented.

Further research is also needed to better understand the extent to which a change to material behavior can be attributed to the change in specific volume and/or the change to state parameter. That research may also show which other property or state changes must be accounted for to attain a complete understanding. The evolution of the pore size distribution may be of critical importance as it has a major influence on the evolution of the microstructure. Alterations in microstructure could potentially lead to variations in mechanical behavior.

5 Conclusions

Results of erosion tests and triaxial tests conducted on a gap-graded cohesionless soil have been presented.

The erosion characteristics, especially flow rate and cumulative eroded soil mass, were influenced by the hydraulic gradient, confining stress and initial relative density. The flow rate decreased with the increase in initial relative density or effective confining stress, and increased with the increase in hydraulic gradient. The cumulative eroded soil mass also increased with the increase in hydraulic gradient, and decreased with the increase in initial density and effective confining stress.

The stress–strain behaviors, and related mechanical properties, after different amounts of erosion were also investigated. The critical state friction angle remained constant for the soil, whatever the amount of erosion. The peak deviator stress and peak friction angle, however, tended to decrease as the amount of erosion increased. The volumetric strain at large shear strain decreased as the amount of erosion increased. The erosion also caused the critical state line to move upwards in the compression plane. The upward movement was less than the increase in void ratio due to erosion, with the overall affect being an increase in state parameter (i.e., a less negative value) and a tendency for the soil behavior to become more like that for a loose condition. These findings help us understand the mechanical consequences of internal erosion on soils and will be useful when developing constitutive models considering internal erosion.

Acknowledgements The authors gratefully acknowledge financial assistance provided by the Australia Research Council (ARC) through a Discovery Project (DP150104123) and Future Fellowship (FT200100820), the National Natural Science Foundation of China (52308370) and the China Scholarship Council.

Funding Open Access funding enabled and organized by CAUL and its Member Institutions.

Data availability statement All experimental data that support the findings of this study are available from the first author upon reasonable request.

Declarations

Conflict of interest The authors declare that they have no conflict of interest.

Open Access This article is licensed under a Creative Commons Attribution 4.0 International License, which permits use, sharing, adaptation, distribution and reproduction in any medium or format, as long as you give appropriate credit to the original author(s) and the source, provide a link to the Creative Commons licence, and indicate if changes were made. The images or other third party material in this article are included in the article's Creative Commons licence, unless indicated otherwise in a credit line to the material. If material is not included in the article's Creative Commons licence and your intended use is not permitted by statutory regulation or exceeds the permitted use, you will need to obtain permission directly from the copyright holder. To view a copy of this licence, visit <http://creativecommons.org/licenses/by/4.0/>.

References

- Alvarado G, Liu N, Coop MR (2012) Effect of fabric on the behaviour of reservoir sandstones. *Can Geotech J* 49(9):1036–1051. <https://doi.org/10.1139/t2012-060>
- ASTM D7181-20 (2020) Test Method for Consolidated Drained Triaxial Compression Test for Soils. ASTM International, West Conshohocken. <https://doi.org/10.1520/D7181-20>
- ASTM D5253-16e1 (2019) Standard Test Methods for Maximum Index Density and Unit Weight of Soils Using a Vibratory Table. ASTM International, West Conshohocken. <https://doi.org/10.1520/D4253-16E01>
- ASTM D5254-16 (2016) Standard Test Methods for Minimum Index Density and Unit Weight of Soils and Calculation of Relative Density. ASTM International, West Conshohocken. <https://doi.org/10.1520/D4254-16>
- Bandini V, Coop MR (2011) The influence of particle breakage on the location of the critical state line of sands. *Soils Found* 51(4):591–600. <https://doi.org/10.3208/sandf.51.591>
- Been K, Jefferies MG (1985) A state parameter for sands. *Géotechnique* 35:99–112. <https://doi.org/10.1680/geot.1985.35.2.99>
- Bendahmane F, Marot D, Alexis A (2008) Experimental parametric study of suffusion and backward erosion. *J Geotech Geoenviron Eng* 134:57–67. [https://doi.org/10.1061/\(ASCE\)1090-0241\(2008\)134:1\(57\)](https://doi.org/10.1061/(ASCE)1090-0241(2008)134:1(57))
- Burenkova VV (1993) Assessment of suffusion in non-cohesive and graded soils. In: *Filters in geotechnical and hydraulic engineering*, Balkema, Rotterdam, pp 357–360
- Cavarretta I, Coop MR, O'Sullivan C (2010) The influence of particle characteristics on the behaviour of coarse grained soils. *Géotechnique* 60(6):413–423. <https://doi.org/10.1680/geot.2010.60.6.413>
- Chang CS, Yin ZY (2011) Micromechanical modeling for behavior of silty sand with influence of fine content. *Int J Solids Struct* 48:2655–2667. <https://doi.org/10.1016/j.ijssolstr.2011.05.014>
- Chang DS, Zhang L, Cheuk J (2014) Mechanical consequences of internal soil erosion. *HKIE Trans* 21:198–208. <https://doi.org/10.1080/1023697X.2014.970746>
- Chang DS, Zhang LM (2011) A stress-controlled erosion apparatus for studying internal erosion in soils. *Geotech Test J* 34:103889. <https://doi.org/10.1520/GTJ103889>
- Chang DS, Zhang LM (2013) Critical hydraulic gradients of internal erosion under complex stress states. *J Geotech Geoenviron Eng* 139:1454–1467. [https://doi.org/10.1061/\(ASCE\)GT.1943-5606.0000871](https://doi.org/10.1061/(ASCE)GT.1943-5606.0000871)
- Chen F, Jiang S, Xiong H, Yin ZY, Chen X (2023) Micro pore analysis of suffusion in filter layer using tri-layer CFD–DEM model. *Comput Geotech* 156:105303. <https://doi.org/10.1016/j.compgeo.2023.105303>
- Chu J (1995) An experimental examination of the critical state and other similar concepts for granular soils. *Can Geotech J* 32:1065–1075. <https://doi.org/10.1139/t95-104>
- Ciantia MO, Arroyo M, O'Sullivan C et al (2019) Grading evolution and critical state in a discrete numerical model of Fontainebleau sand. *Géotechnique* 69:1–15. <https://doi.org/10.1680/jgeot.17.P.023>
- Dassanayake SM, Mousa AA, Ilankoon S, Fowmes GJ (2022) Internal instability in soils: a critical review of the fundamentals and ramifications. *Transp Res Rec* 2676:1–26. <https://doi.org/10.1177/03611981211056908>
- Fannin RJ, Slangen P (2014) On the distinct phenomena of suffusion and suffosion. *Géotechnique Lett* 4:289–294. <https://doi.org/10.1680/geolett.14.00051>
- Foster M, Fell R, Spannagle M (2000) The statistics of embankment dam failures and accidents. *Can Geotech J* 37:1000–1024. <https://doi.org/10.1139/t00-030>
- Hicher P-Y (2013) Modelling the impact of particle removal on granular material behaviour. *Géotechnique* 63:118–128. <https://doi.org/10.1680/geot.11.P.020>
- Hu Z, Zhang Y, Yang Z (2020) Suffusion-induced evolution of mechanical and microstructural properties of gap-graded soils using CFD-DEM. *J Geotech Geoenviron Eng* 146:04020024. [https://doi.org/10.1061/\(ASCE\)GT.1943-5606.0002245](https://doi.org/10.1061/(ASCE)GT.1943-5606.0002245)
- Indraratna B, Muttuvel T, Khabbaz H, Armstrong R (2008) Predicting the erosion rate of chemically treated soil using a process simulation apparatus for internal crack erosion. *J Geotech Geoenviron Eng* 134:837–844. [https://doi.org/10.1061/\(ASCE\)1090-0241\(2008\)134:6\(837\)](https://doi.org/10.1061/(ASCE)1090-0241(2008)134:6(837))
- Istomina VS (1957) Filtration stability of soils. *Gostroizdat, Moscow Leningrad (in Russian)*
- Jefferies M, Been K (2015) *Soil liquefaction: a critical state approach*, 2nd edn. CRC Press, Boca Raton
- Kawano K, Shire T, O'Sullivan C (2018) Coupled particle-fluid simulations of the initiation of suffusion. *Soils Found* 58:972–985. <https://doi.org/10.1016/j.sandf.2018.05.008>
- Ke L, Takahashi A (2014) Experimental investigations on suffusion characteristics and its mechanical consequences on saturated cohesionless soil. *Soils Found* 54:713–730. <https://doi.org/10.1016/j.sandf.2014.06.024>
- Ke L, Takahashi A (2014) Triaxial erosion test for evaluation of mechanical consequences of internal erosion. *Geotech Test J* 37:20130049. <https://doi.org/10.1520/GTJ20130049>
- Kenney TC, Lau D (1985) Internal stability of granular filters. *Can Geotech J* 22:215–225. <https://doi.org/10.1139/t85-029>

29. Kenney TC, Lau D (1986) Internal stability of granular filters: reply. *Can Geotech J* 23:420–423. <https://doi.org/10.1139/t86-068>
30. Kézdi A (1979) *Soil physics-developments in geotechnical engineering* 25. Elsevier Scientific Publishing Co., Amsterdam
31. Kokusho T (2000) Correlation of pore-pressure B-value with P-wave velocity and Poisson's ratio for imperfectly saturated sand or gravel. *Soils Found* 40:95–102. https://doi.org/10.3208/sandf.40.4_95
32. Ladd RS (1978) Preparing test specimens using undercompaction. *Geotech Test J* 1:16. <https://doi.org/10.1520/GTJ10364J>
33. Lafleur J, Mlynarek J, Rollin AL (1989) Filtration of broadly graded cohesionless soils. *J Geotech Eng* 115:1747–1768. [https://doi.org/10.1061/\(ASCE\)0733-9410\(1989\)115:12\(1747\)](https://doi.org/10.1061/(ASCE)0733-9410(1989)115:12(1747))
34. Lambe TW, Whitman RV (1991) *Soil mechanics*. Wiley, Chichester
35. Li M (2008) Seepage induced instability in widely graded soils. PhD thesis, University of British Columbia, Vancouver. <https://doi.org/10.14288/1.0063080>
36. Li S (2019) The mechanical consequences of internal erosion on gap-graded soil. PhD thesis, UNSW Sydney
37. Li S, Russell AR, Muir Wood D (2020) Influence of particle-size distribution homogeneity on shearing of soils subjected to internal erosion. *Can Geotech J* 57:1684–1694. <https://doi.org/10.1139/cgj-2019-0273>
38. Li WC, Deng G, Liang XQ et al (2020) Effects of stress state and fine fraction on stress transmission in internally unstable granular mixtures investigated via discrete element method. *Powder Technol* 367:659–670. <https://doi.org/10.1016/j.powtec.2020.04.024>
39. Lubochkov EA (1965) Graphical and analytical methods for the determination of internal stability of filters consisting of non cohesive soil. *Izv Vniig* 78:255–280
40. Luo Y, Luo B, Xiao M (2020) Effect of deviator stress on the initiation of suffusion. *Acta Geotech* 15:1607–1617. <https://doi.org/10.1007/s11440-019-00859-x>
41. McDougall J, Kelly D, Barreto D (2013) Particle loss and volume change on dissolution: experimental results and analysis of particle size and amount effects. *Acta Geotech* 8:619–627. <https://doi.org/10.1007/s11440-013-0212-0>
42. McDougall JR, Kelly D, Barreto D (2019) Particle loss: an initial investigation into size effects and stress-dilatancy. *Soils Found* 59:726–737. <https://doi.org/10.1016/j.sandf.2019.03.002>
43. Mehdizadeh A, Disfani MM, Evans R, Arulrajah A (2018) Progressive internal erosion in a gap-graded internally unstable soil: mechanical and geometrical effects. *Int J Geomech* 18:04017160. [https://doi.org/10.1061/\(ASCE\)GM.1943-5622.0001085](https://doi.org/10.1061/(ASCE)GM.1943-5622.0001085)
44. Moffat R, Fannin RJ (2011) A hydromechanical relation governing internal stability of cohesionless soil. *Can Geotech J* 48:413–424. <https://doi.org/10.1139/T10-070>
45. Moffat R, Fannin RJ, Garner SJ (2011) Spatial and temporal progression of internal erosion in cohesionless soil. *Can Geotech J* 48:399–412. <https://doi.org/10.1139/T10-071>
46. Muir Wood D (1990) *Soil behaviour and critical state soil mechanics*. Cambridge University Press, Cambridge
47. Muir Wood D, Maeda K (2008) Changing grading of soil: effect on critical states. *Acta Geotech* 3:3–14. <https://doi.org/10.1007/s11440-007-0041-0>
48. Muir Wood D, Maeda K, Nukudani E (2010) Modelling mechanical consequences of erosion. *Géotechnique* 60:447–457. <https://doi.org/10.1680/geot.2010.60.6.447>
49. Ouyang M, Takahashi A (2016) Influence of initial fines content on fabric of soils subjected to internal erosion. *Can Geotech J* 53:299–313. <https://doi.org/10.1139/cgj-2014-0344>
50. Papadopoulou A, Tika T (2008) The effect of fines on critical state and liquefaction resistance characteristics of non-plastic silty sands. *Soils Found* 48:713–725. <https://doi.org/10.3208/sandf.48.713>
51. Prasomsri J, Shire T, Takahashi A (2021) Effect of fines content on onset of internal instability and suffusion of sand mixtures. *Géotechnique Lett* 11:209–214. <https://doi.org/10.1680/jgele.20.00089>
52. Rousseau Q, Sciarra G, Gelet R, Marot D (2020) Modelling the poroelastoplastic behaviour of soils subjected to internal erosion by suffusion. *Int J Numer Anal Methods Geomech* 44:117–136. <https://doi.org/10.1002/nag.3014>
53. Russell AR (2014) How water retention in fractal soils depends on particle and pore sizes, shapes, volumes and surface areas. *Géotechnique* 64:379–390. <https://doi.org/10.1680/geot.13.P.165>
54. Sato M, Kuwano R (2016) Effects of internal erosion on mechanical properties evaluated by triaxial compression tests. *Jpn Geotech Soc Spec Publ* 2:1056–1059. <https://doi.org/10.3208/jgssp.JPN-127>
55. Sato M, Kuwano R (2018) Laboratory testing for evaluation of the influence of a small degree of internal erosion on deformation and stiffness. *Soils Found* 58:547–562. <https://doi.org/10.1016/j.sandf.2018.01.004>
56. Scholtès L, Hicher P-Y, Sibille L (2010) Multiscale approaches to describe mechanical responses induced by particle removal in granular materials. *Comptes Rendus Mécanique* 338:627–638. <https://doi.org/10.1016/j.crme.2010.10.003>
57. Sherman WC (1953) *Filter Experiments and Design Criteria*. MS, NTIS AD 771076, U.S. Army Waterways Expert Station, Vicksburg, VA
58. Shire T, O'Sullivan C, Hanley KJ, Fannin RJ (2014) Fabric and effective stress distribution in internally unstable soils. *J Geotech Geoenviron Eng* 140:04014072. [https://doi.org/10.1061/\(ASCE\)GT.1943-5606.0001184](https://doi.org/10.1061/(ASCE)GT.1943-5606.0001184)
59. Sibille L, Marot D, Sail Y (2015) A description of internal erosion by suffusion and induced settlements on cohesionless granular matter. *Acta Geotech* 10:735–748. <https://doi.org/10.1007/s11440-015-0388-6>
60. Skempton AW, Brogan JM (1994) Experiments on piping in sandy gravels. *Géotechnique* 44(3):449–460. <https://doi.org/10.1680/geot.1994.44.3.449>
61. Sufian A, Russell AR, Whittle AJ, Saadatfar M (2015) Pore shapes, volume distribution and orientations in monodisperse granular assemblies. *Granul Matter* 17:727–742. <https://doi.org/10.1007/s10035-015-0590-0>
62. Tomlinson SS, Vaid YP (2000) Seepage forces and confining pressure effects on piping erosion. *Can Geotech J* 37:1–13. <https://doi.org/10.1139/t99-116>
63. Wan CF, Fell R (2004) Investigation of rate of erosion of soils in embankment dams. *J Geotech Geoenviron Eng* 130:373–380. [https://doi.org/10.1061/\(ASCE\)1090-0241\(2004\)130:4\(373\)](https://doi.org/10.1061/(ASCE)1090-0241(2004)130:4(373))
64. Wan CF, Fell R (2008) Assessing the potential of internal instability and suffusion in embankment dams and their foundations. *J Geotech Geoenviron Eng* 134:401–407. [https://doi.org/10.1061/\(ASCE\)1090-0241\(2008\)134:3\(401\)](https://doi.org/10.1061/(ASCE)1090-0241(2008)134:3(401))
65. Xiao M, Shwiyhat N (2012) Experimental investigation of the effects of suffusion on physical and geomechanic characteristics of sandy soils. *Geotech Test J* 35:104594. <https://doi.org/10.1520/GTJ104594>
66. Xu Y, Zhang LM (2009) Breaching parameters for earth and rockfill dams. *J Geotech Geoenviron Eng* 135:1957–1970. [https://doi.org/10.1061/\(ASCE\)GT.1943-5606.0000162](https://doi.org/10.1061/(ASCE)GT.1943-5606.0000162)
67. Yang J, Wei LM (2012) Collapse of loose sand with the addition of fines: the role of particle shape. *Géotechnique* 62(12):111–1125. <https://doi.org/10.1680/geot.11.P.062>
68. Yang J, Luo XD (2015) Exploring the relationship between critical state and particle shape for granular materials. *J Mech*

- Phys Solids 84:196–213. <https://doi.org/10.1016/j.jmps.2015.08.001>
69. Yang J, Luo XD (2018) The critical state friction angle of granular materials: does it depend on grading? *Acta Geotech* 13:535–547. <https://doi.org/10.1007/s11440-017-0581-x>
70. Yang J, Yin ZY, Laouafa F, Hicher P-Y (2019) Internal erosion in dike-on-foundation modeled by a coupled hydromechanical approach. *Int J Numer Anal Methods Geomech* 43:663–683. <https://doi.org/10.1002/nag.2877>
71. Yang Y, Jiang J, Xu C, Mao W (2023) Mechanical behavior of gap-graded soil subjected to internal erosion: comparison of suffusion and concentrated erosion. *Eur J Environ Civ Eng* 10:1–15. <https://doi.org/10.1080/19648189.2023.2247043>
72. Yin ZY, Huang HW, Hicher P-Y (2016) Elastoplastic modeling of sand–silt mixtures. *Soils Found* 56:520–532. <https://doi.org/10.1016/j.sandf.2016.04.017>
73. Yin ZY, Zhao J, Hicher P-Y (2014) A micromechanics-based model for sand-silt mixtures. *Int J Solids Struct* 51:1350–1363. <https://doi.org/10.1016/j.ijsolstr.2013.12.027>
74. Zhang F, Li M, Peng M, Chen C, Zhang L (2019) Three-dimensional DEM modeling of the stress–strain behavior for the gap-graded soils subjected to internal erosion. *Acta Geotech* 14:487–503. <https://doi.org/10.1007/s11440-018-0655-4>

Publisher's Note Springer Nature remains neutral with regard to jurisdictional claims in published maps and institutional affiliations.